Design of Flapping Airfoil for Optimal Aerodynamic Performance in Low-Reynolds Number Flows

Jung-Sang Lee[*]
Seoul National University, Seoul 151-742, Republic of Korea
and
Chongam Kim[†] and Kyu Hong Kim[‡]
*Institute of Advanced Aerospace Technology, Seoul National University,
Seoul 151-742, Republic of Korea*

Unsteady, viscous, incompressible flows over an airfoil under flapping motion are numerically investigated. Depending on key parameters such as Reynolds number, reduced frequency, and flapping amplitudes, a flapping airfoil could experience complex flow fields. The trailing-edge vortex plays an important role to induce inverse Kármán-vortex street which is a jetlike flow on the downstream and then generates thrust. And, the leading-edge separation vortex is closely related on the propulsive efficiency. Through careful computations of several pitching, plunging, and plunging combined with pitching modes in terms of flow and/or geometry parameters, the key physical flow phenomenon dictating the aerodynamic characteristics of flapping airfoil is identified. Based on the analysis of thrust coefficient and propulsive efficiency a new airfoil shape for optimal aerodynamic performance is proposed. The improved performance of the new flapping airfoil is validated in terms of thrust coefficient and propulsive efficiency in various low-Reynolds number flow regimes.

Nomenclature

C_d	=	drag coefficient
C_l	=	lift coefficient
C_m	=	moment coefficient
C_t	=	thrust coefficient, $-C_d$
c	=	chord length
f	=	frequency, Hz
h	=	plunging amplitude in terms of c
h_{te}	=	plunging amplitude of the trailing edge in terms of c
k	=	reduced frequency in terms of c, $2\pi f c / U_\infty$
Re	=	Reynolds number, $U_\infty c / v_\infty$
S_t	=	Strouhal number, $k h_{te} / \pi$
t	=	time
U_∞	=	freestream velocity
v_∞	=	freestream kinetic viscosity
α_e	=	effective angle of attack
α_0	=	pitching amplitude
η	=	propulsive efficiency
τ	=	pseudotime

Introduction

FLAPPING is considered a natural means of motion among many creatures such as birds and insects. Recently, it became a very interesting research topic due to the applicability to the design of a micro-aerial vehicle or fishlike propulsion system. The force generation mechanism of flapping motion is based on unsteady flow physics. It is closely related to complex nonlinear flow physics such as vortex shedding and dynamic stall and completely different from the force generation in a conventional aircraft.

From the first explanation on the thrust produced by flapping airfoil in 1909 by Knoller, several researchers have investigated this area. And, the crucial mechanism of flapping motion was uncovered in 1935 by Von Kármán and Burgers. They successfully explained that drag or thrust production is based on the pattern of vortex street [1,2]. As shown in Fig. 1, Kármán-vortex street on the downstream side of the airfoil produces drag. When flow condition meets certain criteria, however, an inverse Kármán vortex is introduced and thrust is generated as shown in Fig. 2. Inverse Kármán vortex induces a jetlike flow field, and, as a result, flow gains some momentum and it feeds reaction force back to the airfoil, which is referred to as thrust. Recently further works on flapping airfoil have been conducted by various researchers. Koochesfahani [3] observed the existence of axial flow in the core of wake vortices through water channel experiments. Anderson et al. [4] conducted experimental studies through force and power measurements, as well as visualization data, to classify the principal flow characteristics around and in the wake of the oscillating foil. They found out the conditions for optimal production of thrust when center of pitching is 1/3 chord. Jones and Platzer [1,2] and Jones et al. [5] studied numerically using an unsteady 2-D panel code with a boundary-layer solver for several motion modes. This potential theory, however, is not accurate enough to explain large amplitude motion cases, where massive flow separation and viscous effects are critical. Isogai et al. [6] adopted a compressible Navier–Stokes code with an algebraic turbulence model to take into account the effect of dynamic stall. They concluded that there exist certain conditions related to the phase angle between pitching and plunging motion and reduced frequency, which guarantees the maximum propulsion. Thus, if these conditions are not satisfied, propulsive efficiency is rapidly degraded by the occurrence of large-scale leading-edge separation. Tuncer and Platzer [7] demonstrated a flow visualization using particle tracing and a thin-layer compressible Navier–Stokes code. Based on flow separation characteristics and wake profile, it was concluded that higher propulsive efficiency is associated with attached flows over the full period of oscillatory cycle. Ramamurti and Sandberg [8] calculated aerodynamic coefficients on unstructured triangular mesh by an unsteady

[*]Graduate Student, Ph.D. candidate, School of Mechanical and Aerospace Engineering.
[†]Associate Professor, School of Mechanical and Aerospace Engineering; chongam@snu.ac.kr. Member AIAA.
[‡]Assistant Professor, School of Mechanical and Aerospace Engineering. Member AIAA.
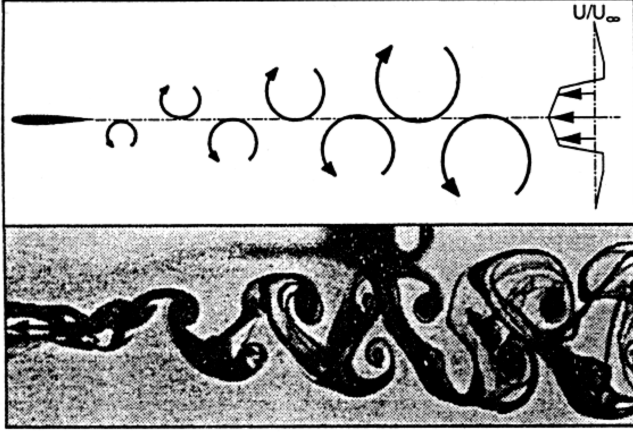
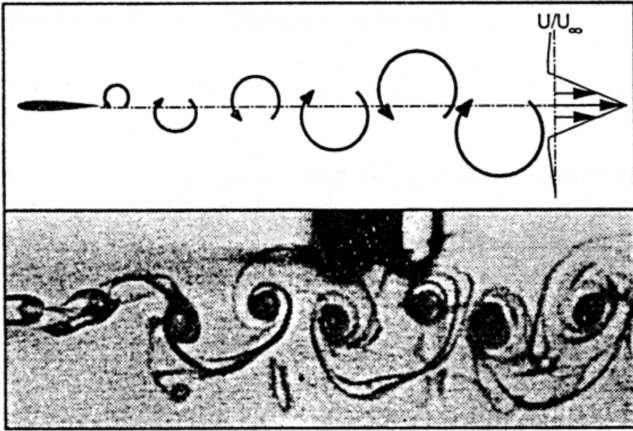**Fig. 1 Drag-inducing vortex street [2].**

Fig. 2 Thrust-inducing vortex street [2].

incompressible viscous solver. From various numerical results, it was observed that thrust coefficient attains the maximum value when pitching leads plunging motion by 120 deg, and the maximum propulsive efficiency is achieved when phase difference is 90 deg.

If a flapping airfoil is regarded as a propulsion device in low-Reynolds number regime, thrust coefficient and propulsive efficiency are generally chosen as major design parameters of flapping airfoil. The mentioned previous researchers mainly focused on propulsive efficiency of flapping motion, of which parameters include phase angle, reduced frequency, and so on. Relatively little attention to thrust coefficient has been paid. Thus, there are lots of cases where thrust coefficient is not sufficient even though propulsive efficiency is high enough. In the present paper, we attempt to improve thrust coefficient as well as propulsive efficiency by designing the flapping airfoil shape itself. Firstly, we conduct numerical experiments at various amplitudes and frequencies using several baseline airfoils. Based on physical observation gained through numerical studies, a role of leading-edge vortex and trailing edge vortex on aerodynamic force enhancement mechanism is observed especially in plunging combined with pitching motion. Also, it is shown that dynamic stall (leading-edge vortex) acts as a thrust enhancement mechanism as well as a lift enhancement mechanism. Finally, through extensive analyses of flapping airfoil, we could come up with a new kind of tadpole-shape airfoil which exhibits enhanced aerodynamic performances.

The present paper is organized as follows. Firstly, numerical methods and the validation of a baseline unsteady incompressible Navier–Stokes code are given. After that, physical investigations on the aerodynamic features of airfoil under pitching, plunging, and flapping motion (plunging combined with pitching) are introduced. And at last, we propose a new flapping airfoil by combining thicker and thinner baseline airfoil, and validate its superior performance in low-Reynolds number flows.

Numerical Methods

The flow field is described by the two-dimensional unsteady incompressible Navie--Stokes equations of the following form.

$$\frac{D\vec{v}}{Dt} + \vec{v}_a \cdot \nabla\vec{v} + \nabla p = \nabla \cdot \sigma \qquad (1a)$$

$$\frac{D\vec{v}}{Dt} = \frac{\partial \vec{v}}{\partial t} + \vec{w} \cdot \nabla\vec{v} \qquad (1b)$$

$$\nabla \cdot \vec{v} = 0 \qquad (1c)$$

where p denotes the pressure and $\vec{v}_a = \vec{v} - \vec{w}$ is the advection velocity vector. Here, $\vec{v}$ is flow velocity, $\vec{w}$ is mesh velocity, and σ is the stress tensor. Both pressure and stress tensors are normalized by density.

Velocity and pressure field are updated iteratively to satisfy Eq. (1a). To relate pressure field with velocity, the pseudocompressibility form [9] of Eq. (2) is employed.

$$\frac{\partial p}{\partial \tau} = -\beta \nabla \cdot \vec{v} \qquad (2)$$

And then, upwind-biased Osher's flux difference splitting is used for spatial discretization. A third-order linear variable reconstruction is introduced to attain higher order spatial accuracy. For time integration, Yoon's lower upper–symmetric gauss seidal [10] is used together with dual time stepping method. The final discretized form of the governing equations is shown in Eq. (3). Here, superscript n is physical time level, and m denotes pseudotime iteration level. $\hat{R}$ is the residual vector, $\hat{S}$ is an unsteady sourcelike term, Q is the variable vector, and J is jacobian. Detailed numerical process including spatial discretization and time integration can be found in [11,12].

$$\left[\frac{I}{J\Delta\tau} + \left(\frac{\partial\hat{R}}{\partial Q} + \frac{\partial\hat{S}}{\partial Q}\right)^{n+1,m}\right]\Delta Q^{n+1,m} = -(\hat{R}^{n+1,m} + \hat{S}^{n+1,m}) \quad (3)$$

To examine the effect of turbulence, a baseline shear-stress transport (SST) [13] and a low-Reynolds number k–ω model [14] are implemented. Boundary conditions used for inflow and outflow regions are based on the method of characteristics and applied explicitly. At inflow, there is one characteristics wave traveling out of the computational domain and two traveling into the domain. Thus, velocity components are specified from the freestream conditions and pressure is extrapolated from interior points. Similarly, at outflow, pressure is specified and velocity components are determined by extrapolation. It should be noted that velocity components are the approximation of Riemann invariants corresponding to the characteristic waves. On the solid wall, velocity is the same as airfoil velocity to reflect time-dependent motion. Pressure on the wall is evaluated from the normal momentum equation. To reduce CPU time required for unsteady viscous flow computations, the baseline code is parallelized by MPI programming method.

Flapping Motion Definition

The flow region of interest is the low-Reynolds number region of $Re = \mathcal{O}(10^3)$–$\mathcal{O}(10^5)$ where flapping motion is usually observed. Generally, flapping motion can be analyzed by dividing into plunging and pitching motion which can be represented by $y(t)$ and $\alpha(t)$, respectively.

$$y(t) = h_0 \sin(kt) \qquad (4a)$$

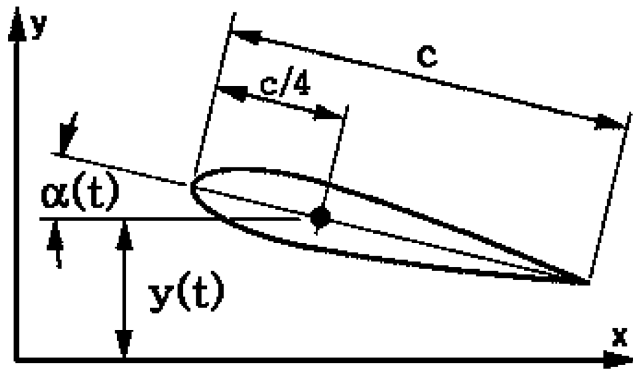$$\alpha(t) = \alpha_0 \sin(kt + \phi) \qquad (4b)$$

Fig. 3 Schematic of airfoil flapping motion.

Here, h_0 denotes plunging motion amplitude and ϕ is a phase angle difference between plunging and pitching motion. Airfoil is located at a body-centered inertial frame of reference that pitches with respect to quarter-chord point. Figure 3 shows the schematic of flapping motion. For the calculation of flapping motion, we adopt a dynamic grid system undergoing rigid body motion because the inner grid points of computational domain do not experience a relative motion.

Code Validation

The baseline code has been validated for the laminar flow over the NACA0012 airfoil under pure pitching motion. Because of the lack of available measurement and flow visualization data for flapping airfoil in low-Reynolds number flow conditions, computational results by Liu and Kawachi [15] based on an incompressible laminar Navier–Stokes solver using artificial compressibility method are chosen for code validation. Here, pitching amplitude is 7.75 deg at $Re = 7200$, and the Strouhal number is taken to vary from 0.05 to 0.4 with an increment of 0.05. The Strouhal number should be defined using reduced frequency and wake diameter in wake region. However, wake diameter cannot be measured simply by numerical or experimental approach. Thus, the Strouhal number is defined using the maximum trailing-edge displacement h_{te} as in [2,8]. A 299×81 C-grid with wall spacing of 5×10^{-4} chord is used, and the outer boundary is extended to 20 chords. To obtain sufficient periodic behavior of aerodynamic coefficient, computations are carried out for 7–9 cycles in accordance with flapping condition. A physical time is obtained by dividing one cycle into 1000 times in all computations. The pseudocompressibility parameter β is set to 200 for all computations. Convergence characteristics are sensitive to the value of β. The present code converged well for the β of 200 through all numerical tests. At each physical time step, pseudoiterations are carried out until both the maximum divergence of velocity and the maximum residual are less than 5×10^{-5} and the maximum subiterations are limited to be less than 10,000 counts. And then, aerodynamic coefficients and performance characteristics are evaluated by averaging time-varied coefficients in the last two cycles. For example, the time-averaged thrust coefficient is defined by Eq. (5). Here c_d is instantaneous drag coefficient that varies with time. And t_{st} and t_{et} denote the start and end time of the last two cycles. And here, the negative value of time-averaged drag coefficient indicates mean thrust coefficient.

$$\bar{c}_t = -\left(\int_{t_{st}}^{t_{et}} c_d \, dt\right)/(t_{et} - t_{st}) \qquad (5)$$

Other mean values of aerodynamic coefficients are also obtained similarly. Figure 4 shows the comparison of mean thrust coefficients with Liu and Kawachi [15]. It is noted that mean thrust coefficient shows a quadratic behavior in terms of the Strouhal number. The effect of turbulence on areodynamic characteristics is also examined. In this case, pitching amplitude is 2 deg at $Re = 1.2 \times 10^4$, and frequency range varies from 0 to 8 by integer number sequence.
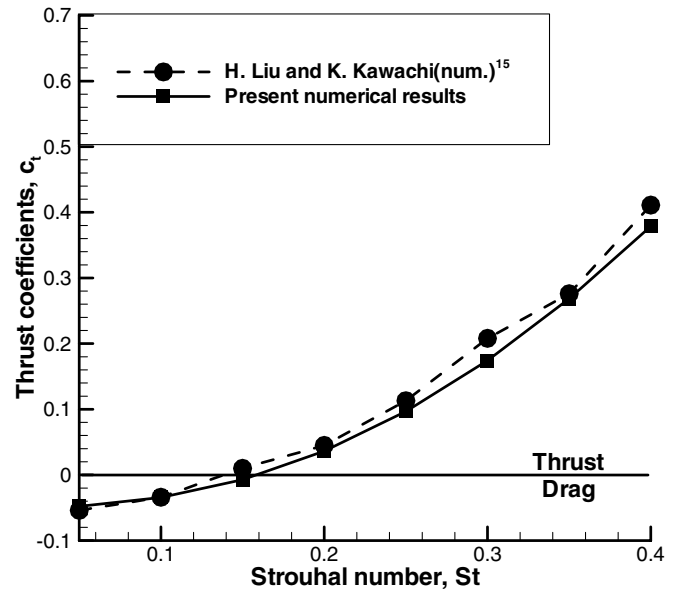
Fig. 4 Variation of thrust coefficient with the Strouhal number ($Re = 7200$).
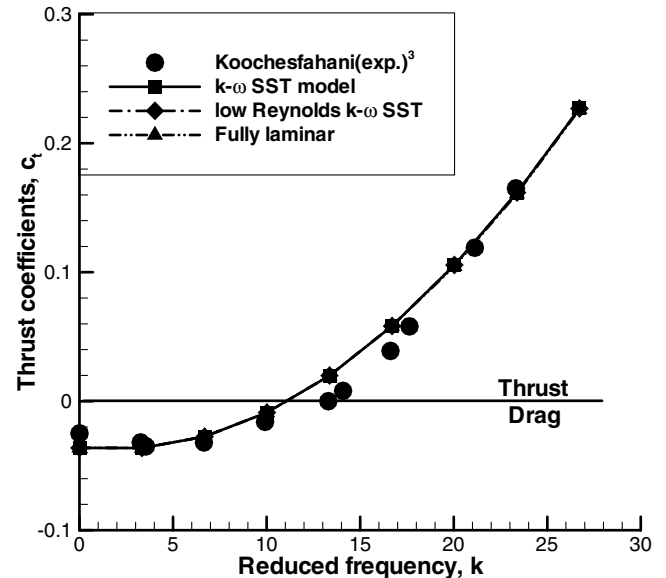
Fig. 5 Variation of thrust coefficient with reduced frequency ($Re = 1.2 \times 10^4$).

Previous works for this flow condition include Koochesfahani's experiment [3]. As shown in Fig. 5, comparison between fully laminar flow and fully turbulent flow by the two-equation k–ω SST model does not yield any noticeable difference. A similar computational investigation can be seen in [6]. Isogai et al. conducted numerical studies by the Baldwin–Lomax algebraic model and fully laminar flow assumption. The additional effect due to low-Reynolds number flow correction in the k–ω model [14] does not seem to be critical in this case either because computed result also yields very similar results to other computations (see Fig. 5). Based on these computations, it is thought that turbulence effect on global aerodynamic coefficients in this flow regime looks very small unlike conventional high-Reynolds number flows. And finally, plunging combined with pitching motion is also simulated. The case of Fig. 7 in [4] is adopted where plunging amplitude is $0.25c$, the maximum angle of attack is 15 deg and phase angle is 90 deg with $Re = 4 \times 10^4$. Numerical simulations are carried out at the Strouhal number of 0.2, 0.4, and 0.6. As shown in Fig. 6, present numerical results show a very good agreement with experimental results.

Numerical Results and Discussions

Thrust Generation

It was reported that two vortices, i.e., leading- and trailing-edge vortices, determine major aerodynamic characteristics of flapping airfoil. As known well, the net thrust force of flapping airfoil is generated by inverse Kármán vortex and a jetlike flow field on the downstream side of trailing edge, whereas Kármán-vortex street is responsible for drag. And large-scale leading-edge vortex is blamed for the decrease of propulsive efficiency. Thus, it is necessary that the effect of each vortex on thrust generation is investigated in detail. In
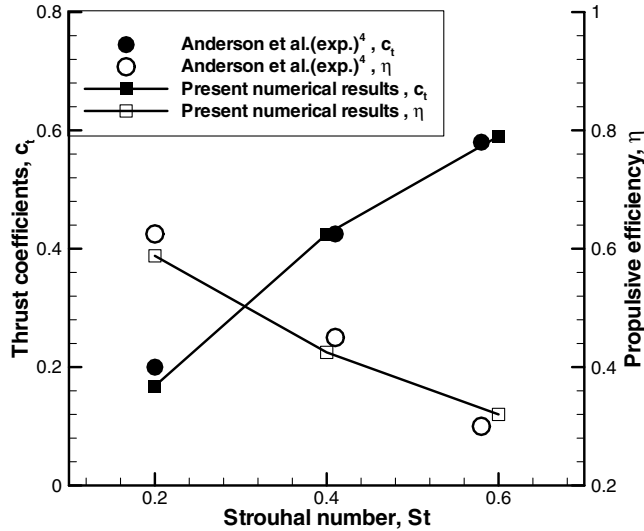
flapping motion with low reduced frequency and high plunging amplitude, the role of leading-edge vortex in the evolution of inverse Kármán vortex was experimentally investigated by Anderson et al. [4]. In the present work, we are more interested in relatively high reduced frequency cases. For identifying the generation mechanism clearly, we separate pitching motion from plunging motion.

Pure Pitching Motion

Pure pitching motion with four different reduced frequencies is simulated at $Re = 5000$. Pitching amplitude is 20 deg., and reduced frequencies are $1, 8, 10$, and 12. The case of $k = 1$ yields net drag, and the other three cases for net thrust force.

Figures 7a–7c show the evolution process of inverse Kármán vortex at high frequency ($k = 10$). The leading-edge vortex is produced at the initial stage of pitch-down motion. The leading-edge vortex does disappear and cannot reach the trailing edge of airfoil. That is, it never interferes with the development of trailing edge vortex which yields inverse Kármán vortex. At the trailing edge, a clockwise rotating flow begins to form and grow (Fig. 7b), and then, it becomes bigger and finally sheds into wake region (see Fig. 7c). During pitch-up motion, a counterclockwise rotating flow develops at trailing edge in a similar fashion. Eventually, those shedding vortices comprise inverse Kármán-vortex street and produce a jetlike flow field. As shown in Fig. 7d, there are two rotating flows around the lower surface of trailing edge at the initial moment of pitch-down motion. One is the larger counterclockwise rotating flow and the other is the smaller clockwise one. At the next stage, the smaller clockwise rotating flow gradually becomes larger to form inverse Kármán vortex while the larger counterclockwise rotating flow is rapidly decayed. Thus, it is expected that the shape of trailing edge directly influences on a thrust because the inverse Kármán vortex is originated from airfoil trailing edge in relatively high reduced frequency. This resembles the formation process of starting vortex around infinite wing very much.
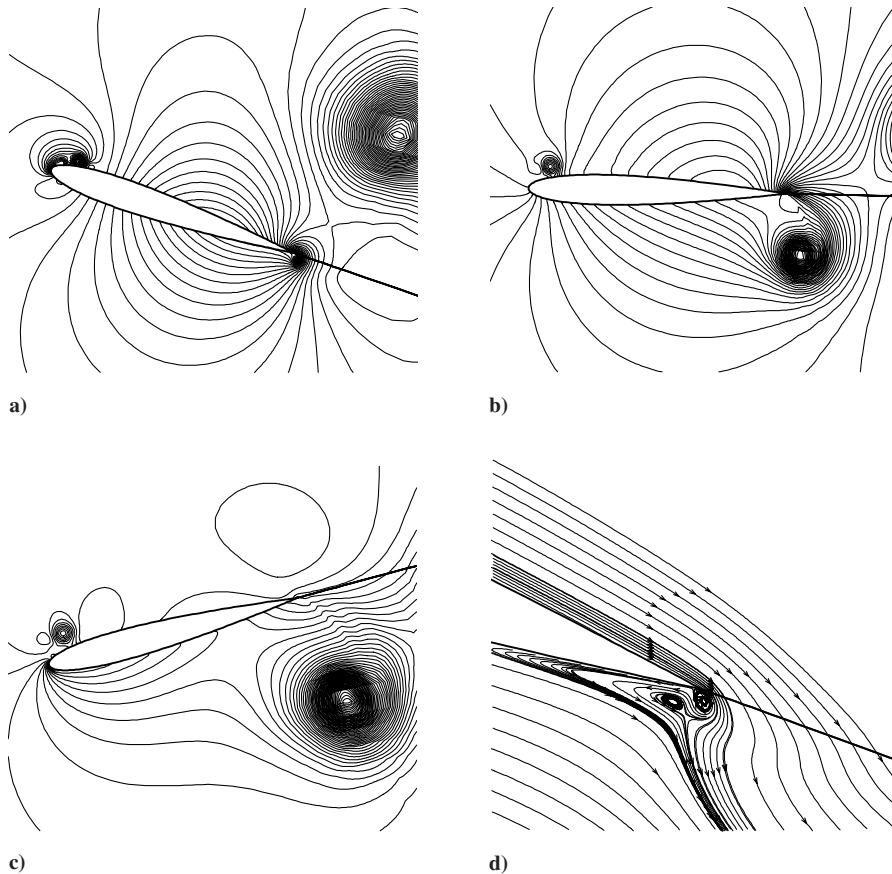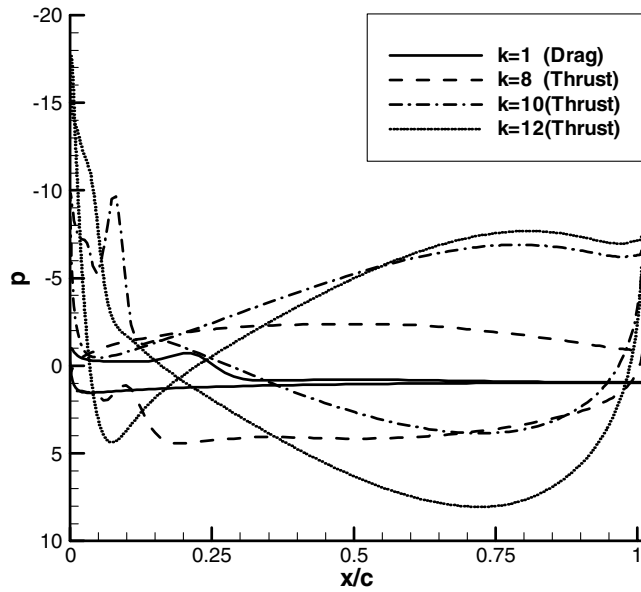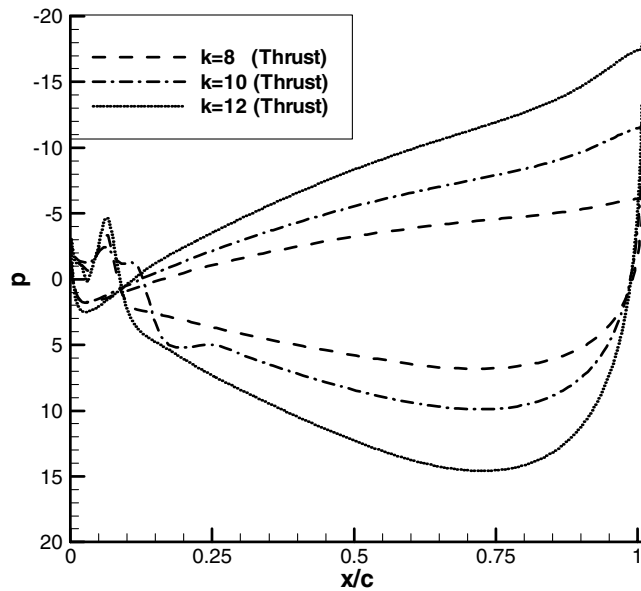

Fig. 6   Variation of thrust coefficient and propulsive efficiency with the Strouhal number ($Re = 4 \times 10^4$).

Fig. 7   Pressure contours in pure pitching motion.

a)

b)

Fig. 8   a) Surface pressure distribution at the instant of inverse Kármán vortex formation (pitching) and b) surface pressure distribution at maximum thrust production (pitching).

Figure 8a shows surface pressure distributions for $k = 1$, 8, 10, and 12 at the instant of inverse Kármán vortex formation that determine the strength of trailing vortex and play a key role in triggering an inverse vortex pattern. Figure 8b shows pressure distributions at maximum thrust (slightly after Fig. 8a). For $k = 1$ (drag generation case), pressure difference between upper and lower surface is negligible, which means the strength of vortex is very weak. On the other hand, for $k = 8$, 10, and 12 (thrust generation cases), noticeable pressure difference is observed. Larger pressure difference yields stronger vortex, which leads to higher thrust. This is shown in Fig. 9. Thus, it is clear that inverse Kármán vortex and a jetlike flow field depend on the intensity of pressure difference around the rear part of airfoil, i.e., the strength of trailing-edge vortex.

Figure 10 shows the typical stability characteristic of pure pitching motion ($k = 10$). Nose-up motion [positive $\alpha(t)$] leads to positive moment coefficient and nose-down motion yields negative value.
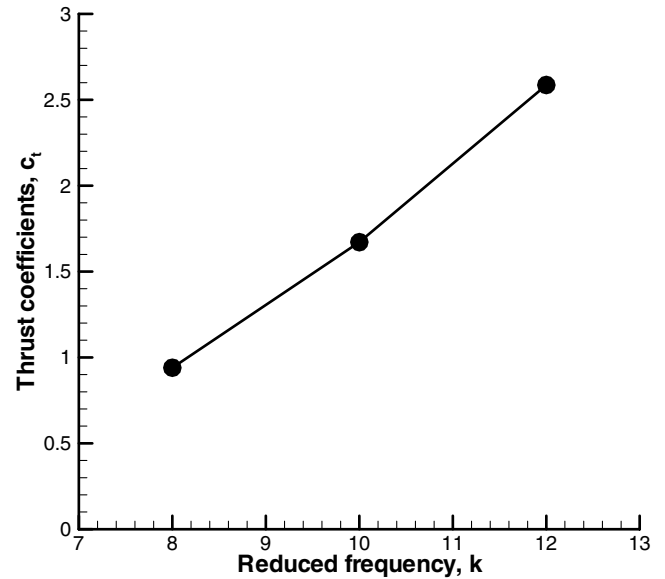

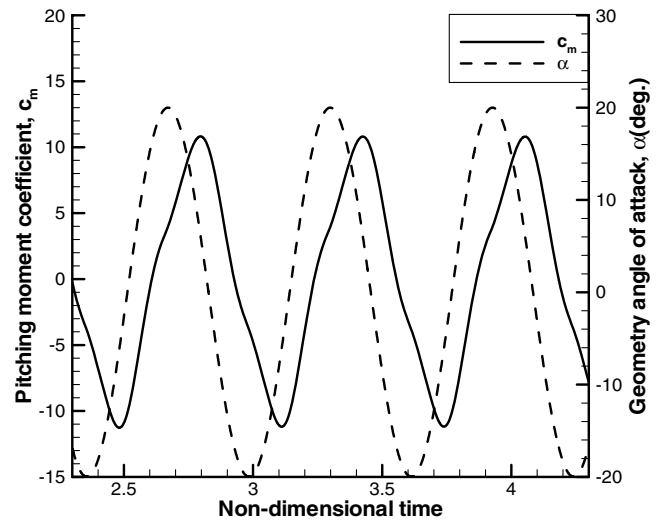**Fig. 9   Variations of c_t with reduced frequency (pitching).**

Fig. 10   Moment coefficient in terms of pitching angle ($k = 8$).

Thus, pure pitching motion without additional stability device or motion mode is considered to be aerodynamically unstable.

Pure Plunging Motion

Similar analysis is carried out for the case of plunging motion. With the same C-grid, four cases of reduced frequencies ($k = 2, 4, 6$, and 8) are calculated at $h = 0.1c$ and $Re = 5000$. At $k = 2$, drag is generated and thrust is observed for the other three cases. Thrust coefficients are shown in Fig. 11 in terms of reduced frequency. Figure 12 shows the typical flow feature of inverse Kármán vortex formation process at high frequency ($k = 6$). Similar to the pitching motion case of high frequency, the leading-edge vortex disappears and the trailing-edge vortex is generated which leads to the inverse Kármán vortex. From the close view around trailing edge, a small counterclockwise rotating vortex is formed firstly and it becomes stronger and is finally shedded. The large clockwise rotating flow is rapidly decayed again. Figure 13 shows pressure distributions at the instant of inverse Kármán vortex formation (Fig. 12a). As confirmed from Figs. 11 and 13, the overall mechanism of inverse Kármán vortex formation in plunging motion depends again on the pressure difference at the rear part of airfoil, i.e., the strength of trailing edge vortex.
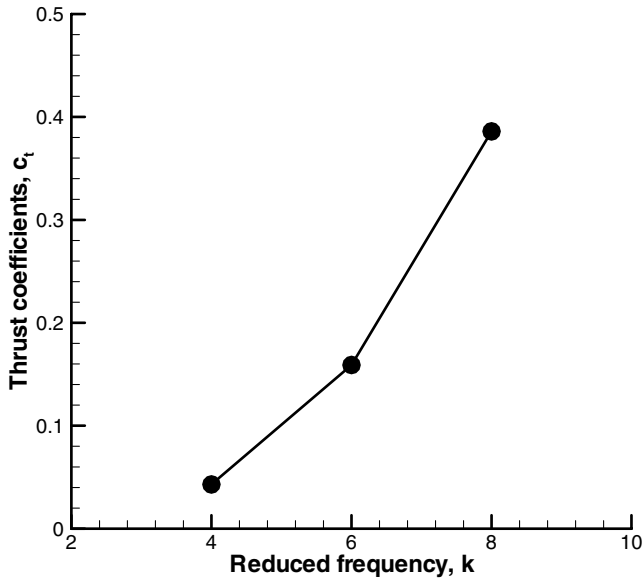
Fig. 11 Variations of c_t with reduced frequency (plunging).

Aerodynamic Force Enhancement

Based on the preceding observation on inverse Kármán vortex formation, we compute unsteady flow fields over flapping airfoil (plunging combined with pitching) at the Reynolds number of 5000, $\alpha_0 = 20$ deg, $h = 0.2c$, $\phi = 90$ deg, and the reduced frequency of $k = 1\text{--}7$.

Figure 14 shows the characteristics of thrust coefficient and propulsive efficiency in terms of reduced frequency. Propulsive efficiency is formally defined as

$$\eta = \bar{c}_t / \bar{c}_p \qquad (6)$$

Here, $\bar{c}_p = -[\int_{t_{st}}^{t_{et}} (\dot{y}c_l + \dot{\alpha}c_m)\,dt]/(t_{et} - t_{st})$ and shown $\bar{c}_t$ is mean thrust coefficient in Eq. (5). $\bar{c}_p$ can be regarded as nondimensional supplied energy to move the airfoil. And, $\dot{y}c_l$ and $\dot{\alpha}c_m$ are instantaneous supplied energy for vertical translation motion (plunging) and angular motion (pitching), respectively.

On thrust coefficient and propulsive efficiency, leading-edge vortex plays an important role. Leading-edge vortex yields pressure suction effect, which eventually leads to thrust coefficient enhancement. It is similar to lift enhancement explained by Ellington et al. [16] They found that leading-edge vortex with sufficient strength on downstroke contributes to higher lift force by
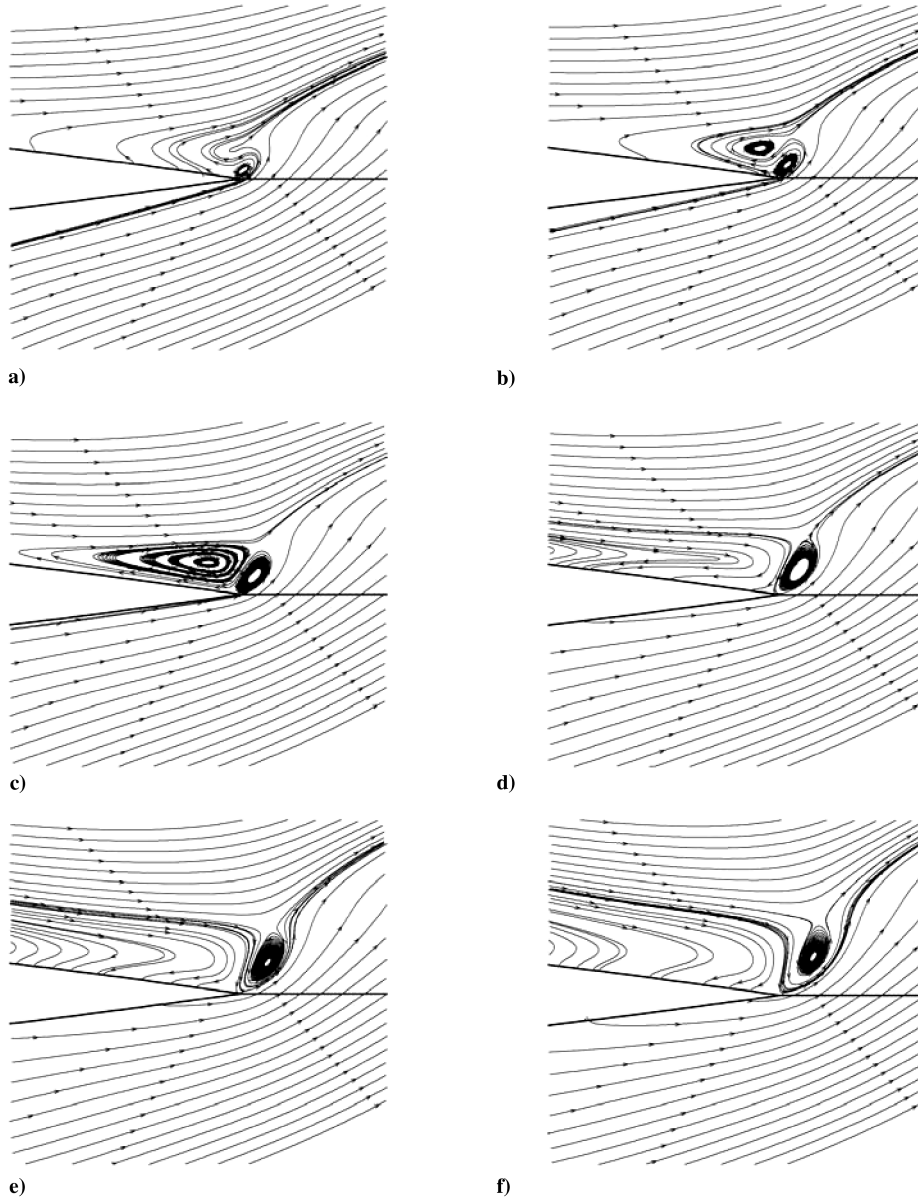

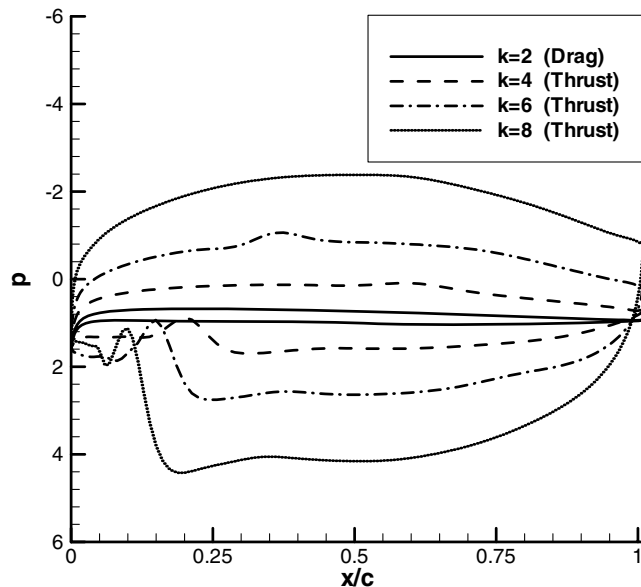Fig. 12 Close-up view of vortex formation at trailing edge (plunging).

Fig. 13 Surface pressure distribution at the instant of inverse Kármán vortex formation (plunging).
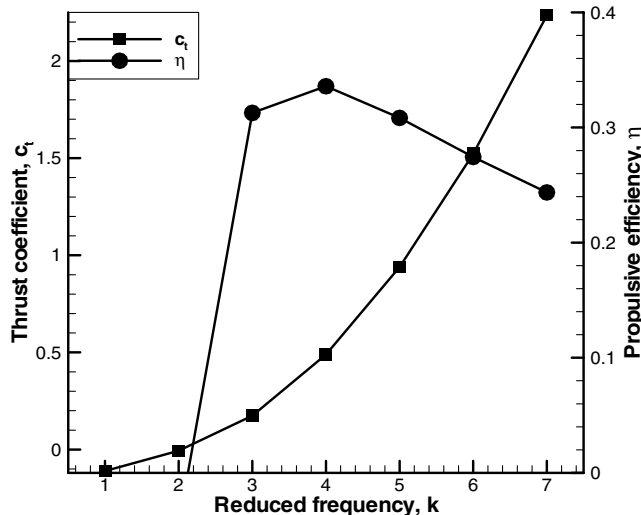

Fig. 15 Variation of thrust and coefficients with non-dimensional time at $k = 7$.

Fig. 14 Variation of thrust coefficient and propulsive efficiency with reduced frequency.

visualizing airflow around the wings of the hawkmoth Manduca sexa and a mechanical model. In other words, leading-edge vortex can be considered as a lift enhancement mechanism on a 3-D insect wing. In 2-D flapping airfoil motion, a similar role of leading-edge vortex in lift enhancement can be observed. Figure 15 shows corresponding aerodynamic behavior. Because of the role of leading-edge vortex, pressure suction region broadens and lift increases consequently. It is, however, noted that thrust also increases, i.e., both thrust and lift increase occur simultaneously, which is clear from Figs. 16. Figure 16a shows pressure field at the peak position during downward and pitch-down motion. And Fig. 16b shows corresponding pressure distribution on the wall. The resultant aerodynamic force is enhanced by pressure suction due to leading-edge vortex developed on the upper surface of airfoil. Thus, its normal component with respect to the freestream direction is nonlinear lift enhancement and horizontal component belongs to thrust (negative drag) enhancement. Similar phenomena can be observed during pitch-up motion. Anderson et al. also found out the leading-edge vortex role of the thrust. They observed the leading-edge vortex can help inverse Kármán vortex formation for the pitching and plunging combined motion in the low reduced frequency [4].
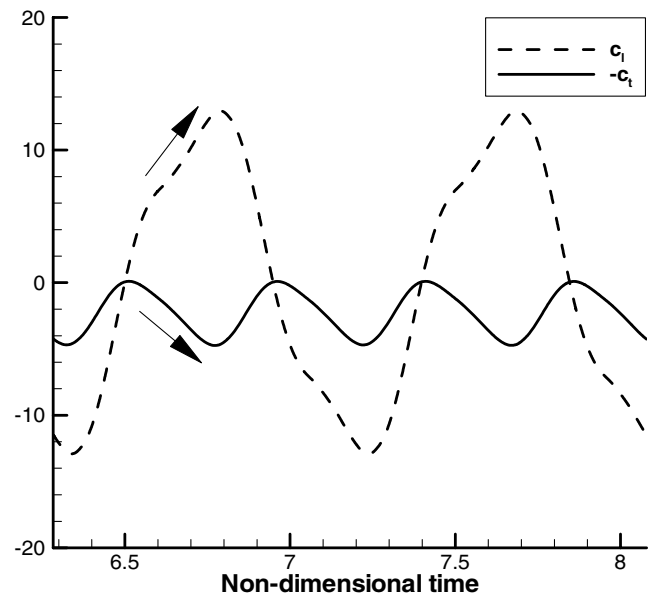
The role of leading-edge vortex, however, is not always beneficial from the viewpoint of propulsive efficiency because additional work has to be done against suction induced by vortex [6]. Concerning leading-edge vortex, the role of phase angle in determining propulsive efficiency is reported by several researchers [6–8]. Especially, Isogai et al. pointed out through numerical study that a large-scale leading-edge vortex can degrade propulsive efficiency, i. e., the strength of leading-edge vortex is related to the reduction of propulsive efficiency.

Figure 14 shows propulsive efficiency in terms of reduced frequency. It reaches the maximal value at the vicinity of $k = 4$ and then it is gradually decreased while thrust coefficient is increased quadratically. It is because the leading-edge vortex becomes stronger with the increase of reduced frequency. At higher frequency, the effective angle of attack, which is defined by Eq. (7) from a quasisteady manner, also increases. As a result, leading-edge vortex becomes stronger.

$$\alpha_e = \tan^{-1}\left(-\frac{\mathrm{d}y}{\mathrm{d}t}\right) + \alpha = \tan^{-1}(-kh\cos kt) + \alpha_0 \sin(kt + \phi)$$

(7)

Figure 17 shows the distribution of effective angle of attack during one flapping cycle. If the vortex is stronger, lift coefficient, which is more dominant in determining propulsive efficiency than thrust coefficient, becomes larger and finally propulsive efficiency is reduced.

When k is below 5, there is no leading-edge vortex. A large-scale leading-edge vortex can be seen only at a relatively high frequency range greater than $k = 6$. In Fig. 18a, flow with $k = 4$ passes smoothly at leading edge and high propulsive efficiency is realized. In the case of $k = 7$ (Fig. 18b), however, a large-scale leading-edge vortex appears and the propulsive efficiency is substantially reduced.

From the observation on the role of leading-edge vortex, it is expected that the possibility of the simultaneous increase of propulsive efficiency and thrust force enhancement is not obvious by changing motion conditions only, because leading-edge vortex shows the positive effect and negative effect simultaneously.

Tadpolelike Airfoil for Shape Optimization

From the preceding results, it can be seen that leading-edge vortex determines the amount of energy needed to sustain flapping motion and that inverse Kármán vortex due to pressure difference between upper and lower near the trailing edge dictates the magnitude of net
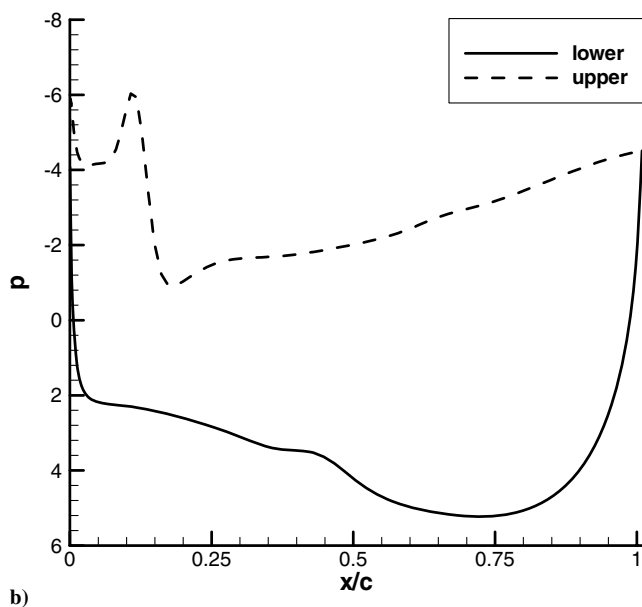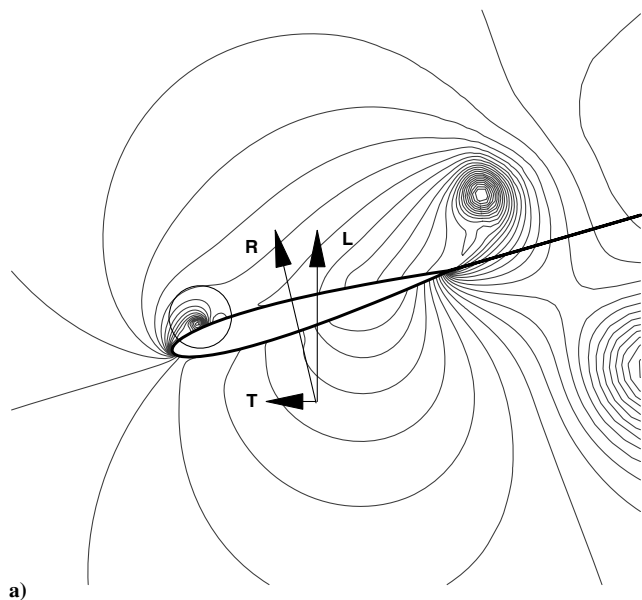
a)

Fig. 17   Behavior of the effective angle of attack.

b)

Fig. 16   a) Pressure contour around flapping airfoil at $k = 7$ and b) surface pressure distribution at $k = 7$.

thrust force. Until recently, the study of flapping motion has been mainly focused on optimal motion condition such as phase angle effect. However, this strategy does not guarantee the simultaneous optimization for thrust and propulsive efficiency. Thus, if we can maintain a situation which yields higher thrust coefficient and lower energy consumption, this would be to realize optimal aerodynamic performance of flapping airfoil. With regard to this issue, the present work is focused on the effect of geometric change on aerodynamic characteristics rather than the effect of motion conditions.

To investigate thickness effect, NACA four-digit airfoils (NACA0009, 0012, 0015) are tested and phase angle is set to 90 deg in all computations. Figure 19 is the comparison of input and output power ratio for each airfoil with the condition of $\alpha_0 = 20$ deg, $h = 0.3c$, $k = 8$, and $Re = 1.2 \times 10^4$ where leading-edge vortex is generated. Here, nondimensional input power is $\bar{c}_p$ and output power is $\bar{c}_t$. Because flow conditions and motion parameters are all the same, comparison is only dependent on the geometric characteristics of each airfoil. In Fig. 19, the thinner airfoil (NACA0009) needs more input power to sustain flapping motion than the thicker one (NACA0015). Thus, the propulsive efficiency of NACA0015 is
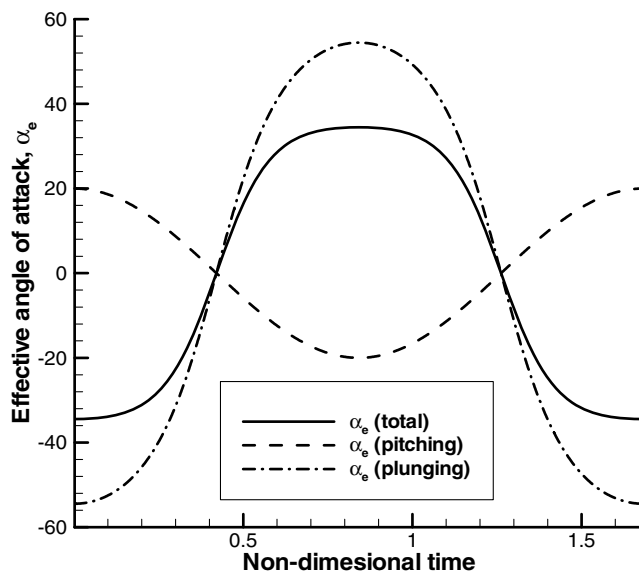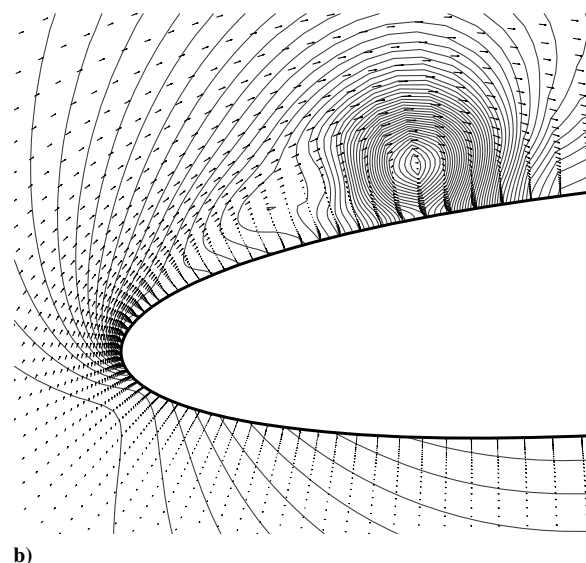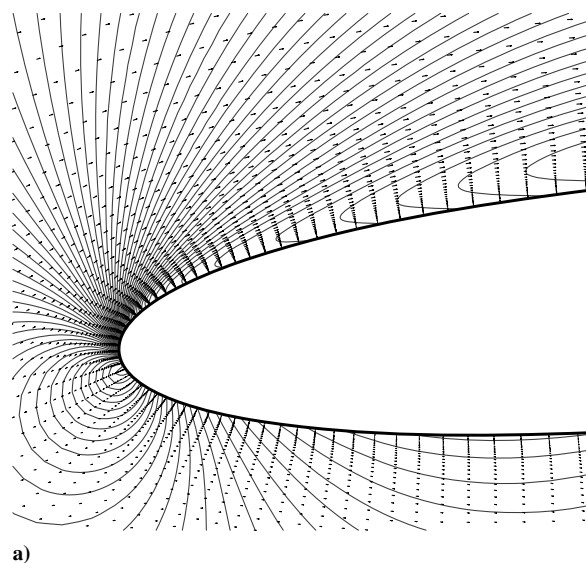

a)

b)

Fig. 18   a) Smooth flow field at $k = 4$ and b) leading-edge separation and vortex formation at $k = 7$.
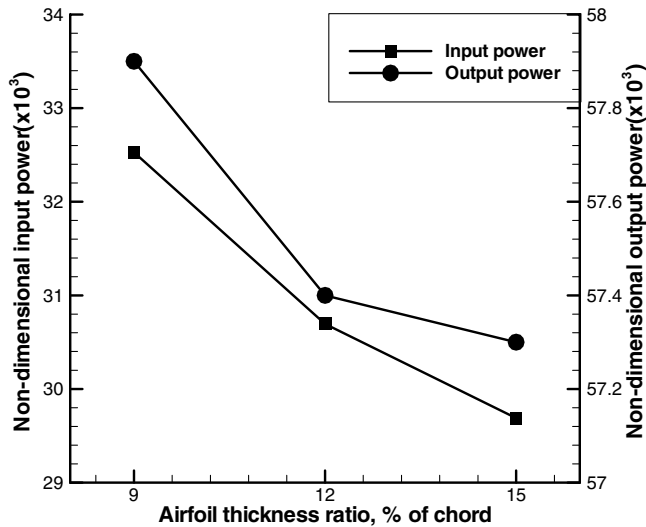
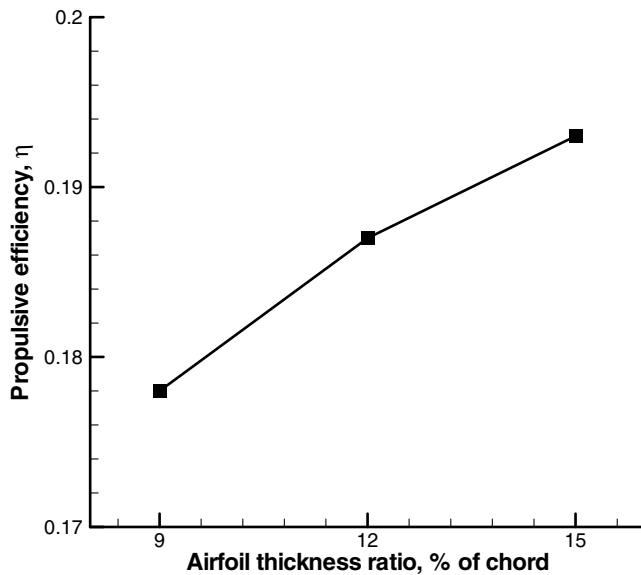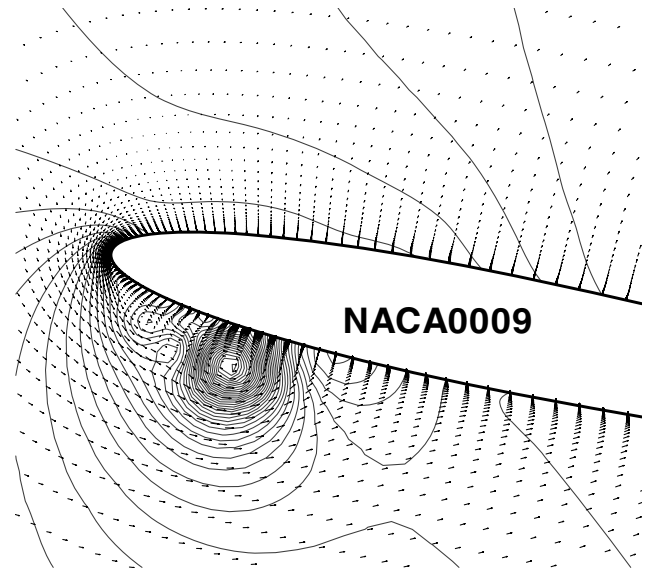Fig. 19   Comparison of input and output powers according to airfoil thickness.

a)

Fig. 20   Comparison of propulsive efficiency according to airfoil thickness.

b)

Fig. 21   a) Leading-edge separation vortex and b) surface pressure distribution (NACA0009).
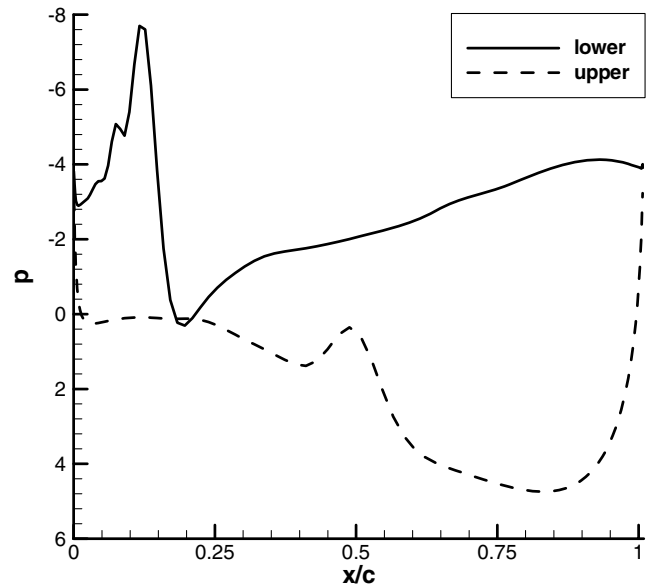
higher than that of NACA0009 (see Fig. 20). It is reasonable that the propulsive efficiency of the thicker airfoil is higher than that of the thinner one when a leading-edge vortex exists.

From Figs. 21a, 21b, 22a, and 22b, it can be seen that the thinner leading edge allows stronger leading-edge vortex formation than the thicker one. Thus, the thinner airfoil experiences larger aerodynamic loads, which leads to larger required input power as shown in Fig. 19. The influence of airfoil thickness on pressure difference around trailing edge is shown in Fig. 23. As mentioned before, pressure difference around trailing edge is directly related to the strength of trailing-edge vortex and the amount of thrust force generation. From Fig. 23, it can be said that the thrust coefficient of the thinner airfoil is higher than that of the thicker one.

In addition to thickness effect, camber is one of the important parameters in determining airfoil geometry. It turns out, through the computational investigations of NACA2412, 4412, and 4612 cases, that camber does not yield positive effect on propulsive efficiency, even though it is really crucial on lift generation. Bird or insect wings actually have camber because lift is also important as well as thrust. In addition, their camber is continuously changed during actual flight mode. Thus, camber effect, combined with 3-D flapping motion and flexible wing structure, has to be explored further. Because the

present paper is concentrated on thrust coefficient and propulsive efficiency in 2-D flapping motion, symmetric airfoils are chosen.

The present research goal is to find an optimal baseline airfoil shape for flapping motion. Previous computations and observations suggest that it is unlikely to achieve maximal thrust force and minimal input power simultaneously by conventional airfoil. Hence, we combine thicker and thinner airfoils to propose a new flapping airfoil, for example, a combination of NACA0015 and NACA0009 as shown in Fig. 24. This combined airfoil resembles a tadpole. And the thicker part is set to be 40% of total chord length from a picture of a tadpole. To clarify its aerodynamic characteristics, two types are considered depending on the shape of trailing edge: one is convex trailing edge (type #1), the other is concave (type #2). The concave model is made by rotating the trailing edge surface of type #1 180 deg.

As mentioned, in case of high frequency, leading-edge vortex cannot reach trailing edge and decays on the surface of airfoil. In case of low frequency, however, leading-edge vortex moves on downstream and interacts with trailing-edge vortex. In the extreme
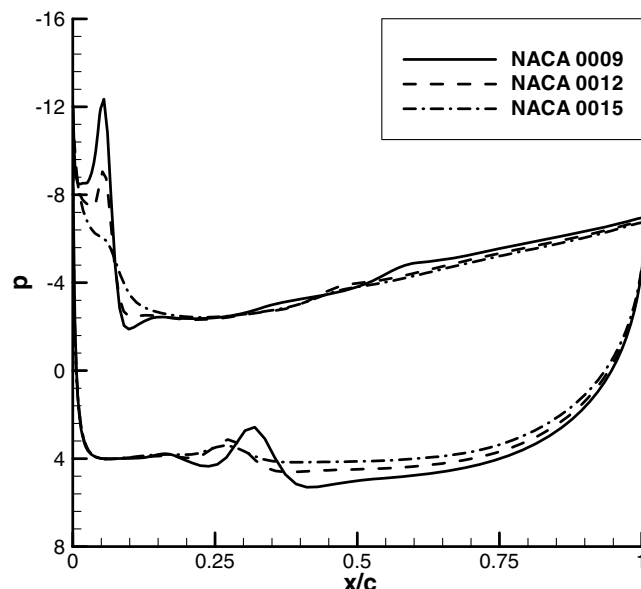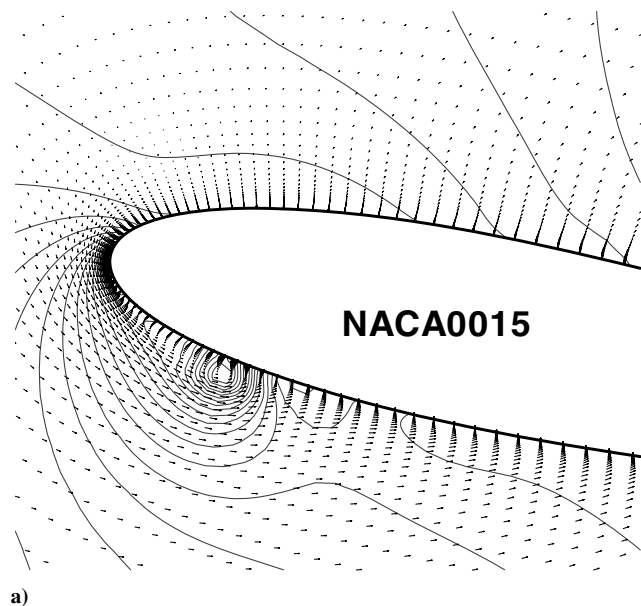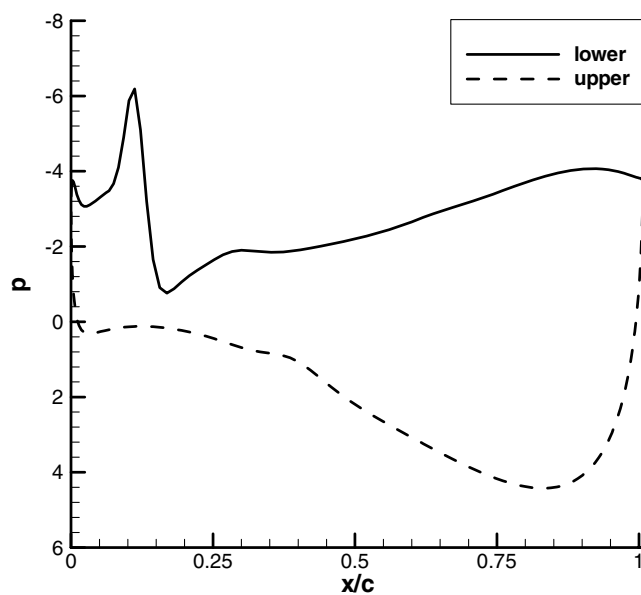
a)

Fig. 23   Surface pressure distribution (flapping).

b)

Fig. 22   a) Leading-edge separation vortex and b) surface pressure distribution (NACA0015).

Fig. 24   Combined airfoil shapes.

case that leading-edge vortex is larger than trailing-edge vortex, leading-edge vortex may cancel out the trailing-edge vortex and drag is generated. Because the role of leading-edge vortex is different, it is necessary to distinguish two cases (high frequency and low frequency).

Firstly, high frequency cases are investigated. For the motion condition of $\alpha_0 = 20 \deg$, $h = 0.4c$, $\phi = 90 \deg$, and $Re = 1.2 \times 10^4$, five airfoils are compared with one another according to reduced frequency which changes from 4 to 8 with an increment of 2. Figures 25 and 26 show the characteristics of the thrust coefficient and propulsive efficiency of each airfoil. It is clearly seen that the performance of modified types #1 and #2 is better in relatively high frequency region ($k = 4$–8). Between modified types #1 and #2, the performance improvement of modified type #2 is higher because trailing edge is designed to be thinner than that of modified type #1 to generate stronger trailing-edge vortex.

Next, for the motion condition of $\alpha_0 = 20 \deg$, $\phi = 90 \deg$, $k = 8$, and $Re = 1.2 \times 10^4$, five airfoils are compared with one another by changing plunging amplitude from 0 to $0.4c$ with an increment of $0.1c$. Plots of the thrust coefficient and propulsive efficiency of each
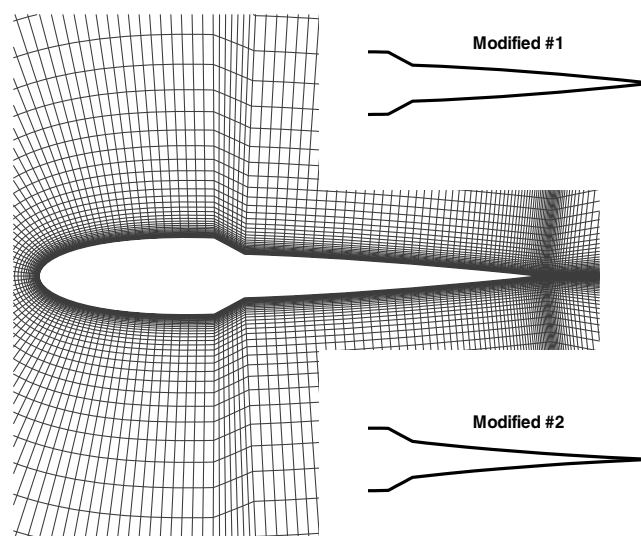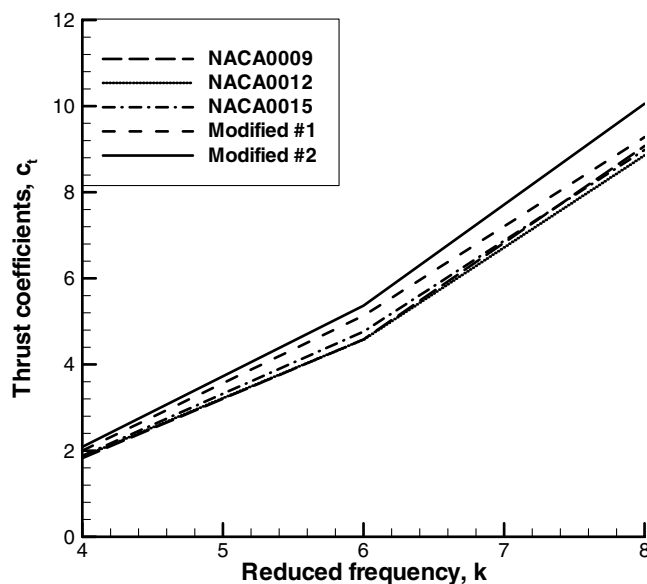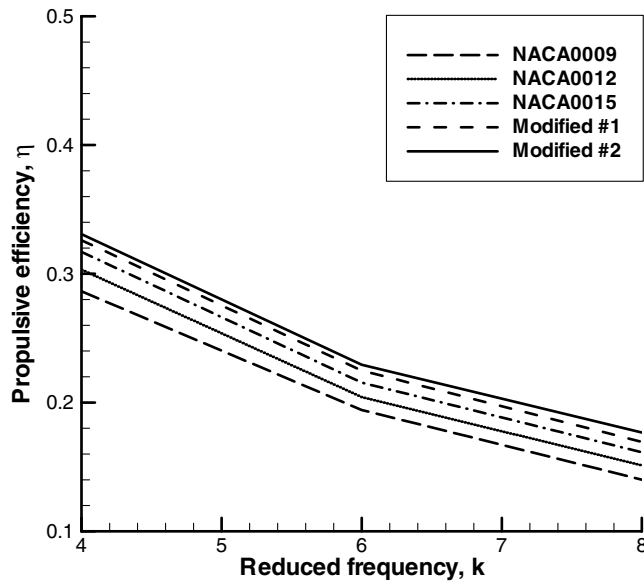

Fig. 25   Thrust coefficient.

Fig. 26   Propulsive efficiency.
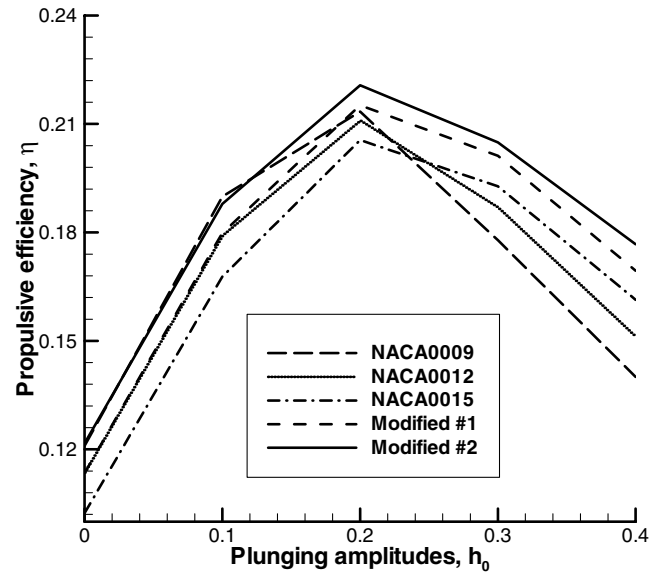

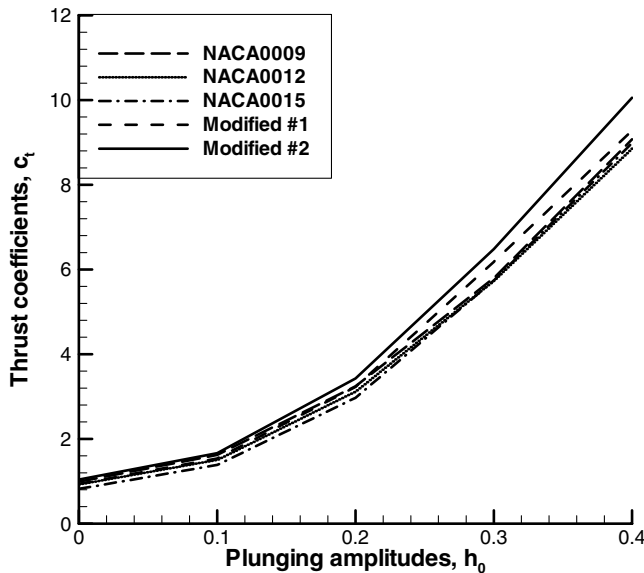**Fig. 28   Propulsive efficiency.**

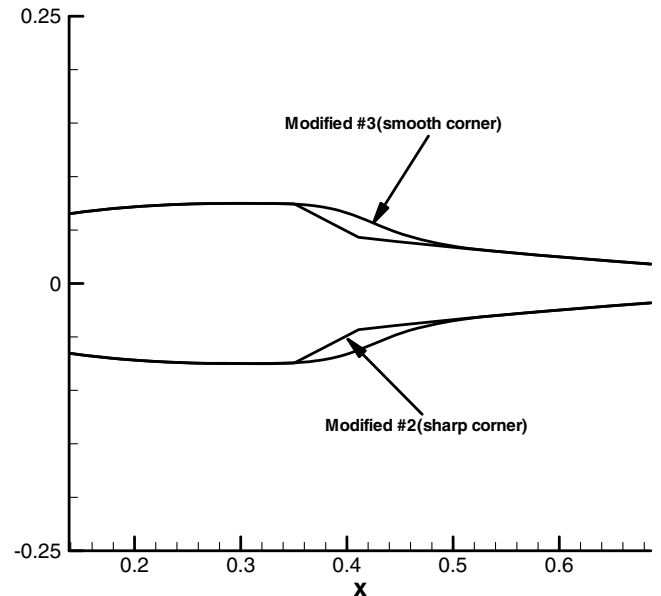**Fig. 27   Thrust coefficient.**

Fig. 29   Modified type #3.

airfoil are shown in Figs. 27 and 28, respectively. Different from Fig. 26, the propulsive efficiency of NACA0015 is not always greater than that of the thinner one (NACA0009). It depends on the existence of leading-edge vortex. In case of low amplitude, there is no leading-edge vortex. Then, the pressure suction effect of the thicker airfoil is larger than that of the thinner one, which reduces propulsive efficiency and therefore the thinner airfoil shows a better efficiency. However, as plunging amplitude increases, leading-edge vortex begins to generate and the behavior of propulsive efficiency is altered accordingly. When h is greater than $0.2c$, the efficiency of thinner airfoil NACA0009 decreases rapidly (see Fig. 28). In case of tadpolelike airfoil, regardless of the existence of leading-edge vortex, modified types #1 and #2 show a better performance in overall plunging amplitude range. Especially, modified type #2 shows again the best performance among the five airfoils.

Secondly, low frequency cases ($k = 0.8$) are also investigated. To obtain the same level of thrust coefficient corresponding to high frequency case, plunging amplitude should be increased accordingly and the effective angle of attack should be large enough. According to the preceding criteria, the case of $\alpha_0 = 30\,\mathrm{deg}$, $h = 2c$, $\phi = 90\,\mathrm{deg}$, and $k = 0.8$ at $Re = 1.2 \times 10^4$ are computed. In this case, however, the original modified types #1 and #2 do not show

better performances compared with other NACA airfoils because geometrical change connecting NACA0015 with NACA0009 is too severe and, as a result, large drag is generated at the connecting region. To prevent this situation, modified type #2 is slightly remodeled by connecting two airfoils more smoothly (see Fig. 29). Figure 30 shows thrust coefficient and propulsive efficiency characteristics of each airfoil. Modified type #3 shows the best performance in terms of thrust coefficient as well as propulsive efficiency. At relatively high-Reynolds number of $Re = 1.2 \times 10^5$ with $\alpha_0 = 40\,\mathrm{deg}$, $h = 2c$, $\phi = 90\,\mathrm{deg}$, and $k = 0.8$, the aerodynamic performance of modified type #3 is also validated. As shown in Fig. 31, the modified airfoil still shows better characteristics then other conventional NACA airfoils. As a result, the aerodynamic merit of the modified airfoil is still observed in the cases of low reduced frequency. And finally, for $\alpha_0 = 20\,\mathrm{deg}$, $h = 0.1c$, $k = 6$, and $\phi = 90\,\mathrm{deg}$ with $Re = 5000$, the aerodynamic performance of each airfoil (NACA0009, 0012, 0015, type #1, type #2, and type #3) is compared again as in Fig. 32. It is noted that the proposed tadpole-shape airfoils yield a better aerodynamic performance.

From the preceding results, we can conclude that the proposed tadpolelike airfoil exhibits a general superiority of aerodynamic
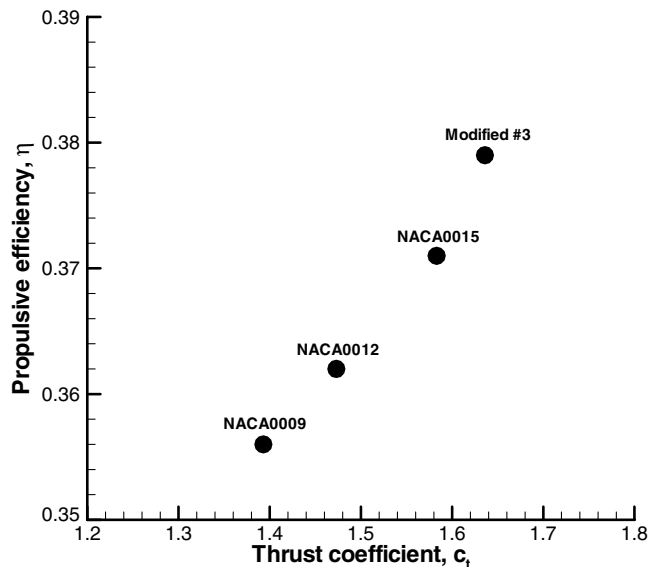
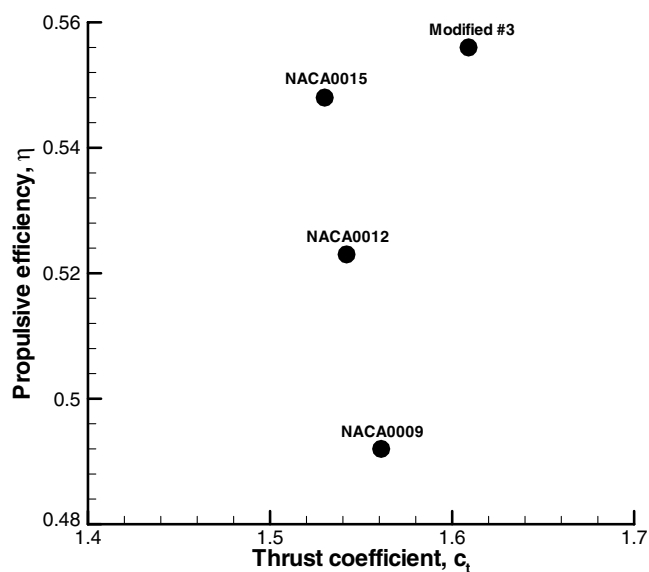**Fig. 30   Thrust coefficient and propulsive efficiency.**

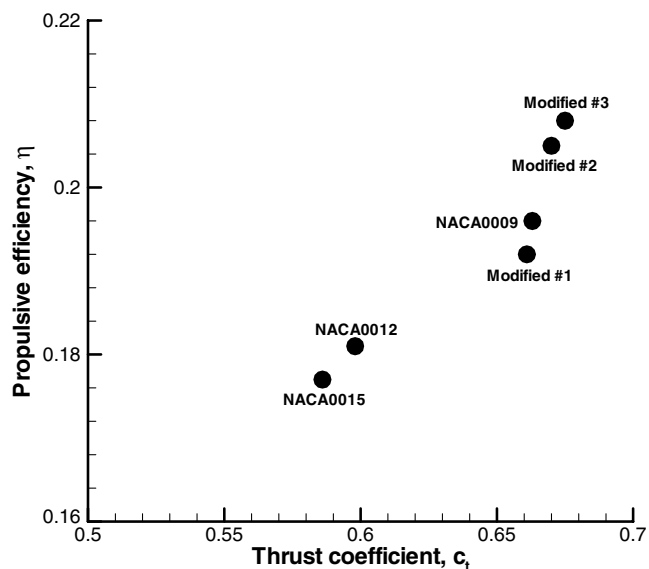**Fig. 31   Thrust coefficient and propulsive efficiency.**

Fig. 32   Thrust coefficient and propulsive efficiency.

performance over a wide range of flow conditions and flapping motions. As a result, it is believed that the proposed tadpolelike airfoil that is made by combining thicker leading edge and thinner trailing edge would be a baseline model for the optimal shape design of flapping airfoil.

Conclusions

Flapping motion can be regarded as a superposition of pitching and plunging motion. From the detailed numerical simulations, it is observed that flow field in flapping motion is governed by two major aerodynamic features. One is leading-edge vortex and the other is trailing-edge vortex. Leading-edge vortex triggers dynamic stall phenomenon and its evolution helps lift enhancement like insects' flight during hovering. Present numerical investigation shows that leading-edge vortex can also provide a thrust enhancement mechanism. However, leading-edge vortex requires additional input power to sustain flapping motion. As a result, it is the direct reason for the decrease of propulsive efficiency. On the other hand, pressure difference between upper and lower surface at trailing edge determines the strength of thrust-generated trailing-edge vortex, i.e., the intensity of inverse Kármán vortex and related jetlike flow fields.

Based on the physical observation from the results of various numerical simulations for flapping airfoil, it is found that the effect of leading and trailing vortices can be favorably combined through geometric modification. Thicker airfoil helps to prevent large-scale vortex formation at leading edge and thinner airfoil excites stronger pressure difference at trailing edge. By combining thicker and thinner airfoil, it is possible to obtain enhanced aerodynamic characteristics including higher thrust coefficient and higher propulsive efficiency. The proposed tadpolelike airfoil yields improved aerodynamic performance in the broad range of amplitude, reduced frequency, and Reynolds number. Thus, it can be used as a baseline flapping airfoil for optimal aerodynamic performance.

References

[1] Jones, K. D., and Platzer, M. F., "Numerical Computation of Flapping-Wing Propulsion and Power Extraction," AIAA Paper 97-0826, Jan. 1997.

[2] Jones, K. D., and Platzer, M. F., "An Experimental and Numerical Investigation of Flapping-Wing Propulsion," AIAA Paper 99-0995, Jan. 1999.

[3] Koochesfahani, M. M., "Vortical Patterns in the Wake of an Oscillating Airfoil," *AIAA Journal*, Vol. 27, No. 9, 1989, pp. 1200–1205.

[4] Anderson, J. M., Streitlien, K., Barrett, D. S., and Triantafyllou, M. S., "Oscillating Foils of High Propulsive Efficiency," *Journal of Fluid Mechanics*, Vol. 360, 1998, pp. 41–72.

[5] Jones, K. D., Davids, S., and Platzer, M. F., "Oscillating-Wing Power Generation," FEDSM Paper 99-7050, 1999.

[6] Isogai, K., Shinmoto, Y., and Watanabe, Y., "Effects of Dynamic Stall on Propulsive Efficiency and Thrust of Flapping Foil," *AIAA Journal*, Vol. 37, No. 10, 1999, pp. 1145–1151.

[7] Tuncer, I. H., and Platzer, M. F., "Computational Study of Flapping Airfoil Aerodynamics," *Journal of Aircraft*, Vol. 37, No. 3, 2000, pp. 514–520.

[8] Ramamurti, R., and Sandberg, W., "Simulation of Flow About Flapping Airfoils Using Finite Element Incompressible Flow Solver," *AIAA Journal*, Vol. 39, No. 2, 2001, pp. 253–260.

[9] Chorin, A. J., "A Numerical Method for Solving Incompressible Viscous Flow Problems," *Journal of Computational Physics*, Vol. 2, No. 1, 1967, pp. 12–26.

[10] Yoon, S., and Kwak, D., "Three-Dimensional Incompressible Navier-Stokes Solver Using Lower-Upper Symmetric-Gauss-Seidel Algorithm," *AIAA Journal*, Vol. 29, No. 6, 1991, pp. 874–875.

[11] Rogers, S. E., and Kwak, D., "An Upwind Differencing Scheme for the

Time-Accurate Incompressible Navier-Stokes Equations," *AIAA Journal*, Vol. 28, No. 2, 1990, pp. 253–262.

[12] Kim, C. S., Kim, C., and Rho, O. H., "Parallel Computations of High-Lift Airfoil Flows Using Two-Equation Turbulence Models," *AIAA Journal*, Vol. 38, No. 8, 2000, pp. 1360–1368.

[13] Menter, F. R., "Two-Equation Eddy-Viscosity Turbulence Models for Engineering Applications," *AIAA Journal*, Vol. 32, No. 8, 1994, pp. 1598–1605.

[14] Wilcox, D. C., "Simulation of Transition with a Two-Equation Turbulence Model," *AIAA Journal*, Vol. 32, No. 2, 1994, pp. 247–255.

[15] Liu, H., and Kawachi, K., "A Numerical Study of Undulatory Swimming," *Journal of Computational Physics*, Vol. 155, No. 2, 1999, pp. 223–247.

[16] Ellington, C. P., van den Berg, C., Willmott, A. P., and Tomas, A. L. R., "Leading-Edge Vortices in Insect Flight," *Nature (London)*, Vol. 384, 1996, pp. 626–630.

K. Fujii
Associate Editor